ADVANCED ENERGY MATERIALS
www.advenergymat.de

Visualizing the Dynamic Wetting and Redistribution of Electrolyte in Lean-Electrolyte Lithium-Sulfur Pouch Cells via *Operando* Neutron Imaging

*Liqiang Lu, Nikolay Kardjilov, Xiangqi Meng, Kang Dong, Yaolin Xu, Qingping Wu, Alessandro Tengattini, Lukas Helfen, Jin Yang, Yan Guo, Moritz Exner, Ingo Manke, and Yan Lu**

The lean electrolyte in lithium-sulfur (Li-S) batteries commonly presents inhomogeneous distribution and inadequate electrolyte wetting, resulting in uneven electrochemical reaction interface, suboptimal performance, and cell failure or accelerated degradation. Non-destructive *operando*/in situ methods that can visualize electrolyte wetting and dynamics during cell operation in liquid metal-sulfur batteries have unfortunately not been described. In this study, the *operando* neutron tomography technique is employed to non-destructively visualize and analyze the electrolyte distribution in practical lean-electrolyte double-layer Li-S pouch cells. Through real-time electrolyte observation across different pouch-cell layers, we unambiguously reveal conglomeration and diminishment of unwetted areas during cell rest, leading to localized electrolyte redistribution. Remarkably, discharge/charge processes can enhance electrolyte homogeneity remarkably, boosting the electrochemical activation of sulfur. Unique periodic "breath-in" and "breath-out" behaviors of electrolyte wetting are observed in the dynamic evolution with the status of discharge and charge, which is correlated to the dissolution and precipitation of sulfur species. These results provide solid evidence of an inhomogeneous distribution of lean electrolyte in practical Li-S pouch cells and offer insights into the correlation between electrolyte redistribution and lithium-sulfur (electro-)chemistry. This work develops valuable guidelines for optimizing testing protocols and strategies for electrolyte wetting in Li-S pouch cells and other metal-sulfur batteries.

1. Introduction

Lithium–sulfur (Li-S) batteries are one of the most promising candidates of next-generation batteries owing to their high energy density (>700 Wh kg^{-1} at cell level) than the state-of-the-art lithium-ion batteries (LIBs) (250–300 Wh kg^{-1} at cell level).[1,2] However, the commercialization of Li-S batteries are impeded by a number of formidable fundamental bottlenecks such as the highly insulating nature of sulfur and lithium sulfides,[3,4] "shuttle effect" of dissolved polysulfides in the conventional ether electrolytes,[5–7] volume variations of cathodes, and degradation of lithium anode and electrolyte.[8,9] Moreover, it has been widely realized that the progress made at the materials level with coin cells cannot be easily translated into prototype pouch cells mainly due to practical metrics including the low sulfur content and sulfur loading of cathodes, much excessive use of lithium and electrolyte in cells.[4,10,11] Thus, it

L. Lu, N. Kardjilov, X. Meng, K. Dong, Y. Xu, Q. Wu, Y. Guo, I. Manke, Y. Lu
Institute of Electrochemical Energy Storage
Helmholtz-Zentrum Berlin für Materialien und Energie
Hahn-Meitner-Platz 1, 14109 Berlin, Germany
E-mail: yan.lu@helmholtz-berlin.de

K. Dong
Multi-Disciplinary Research Division
Institute of High Energy Physics
Chinese Academy of Sciences
Beijing 100049, China

The ORCID identification number(s) for the author(s) of this article can be found under https://doi.org/10.1002/aenm.202501324

DOI: 10.1002/aenm.202501324

A. Tengattini, L. Helfen
Institut Laue-Langevin
71 avenue des Martyrs CS 20156, GRENOBLE Cedex 9 38042, France

A. Tengattini
Univ. Grenoble Alpes
Grenoble INP
CNRS
3SR, 1270 Rue de la Piscine, Grenoble 38400, France

A. Tengattini
Institut universitaire de France (IUF)
France

J. Yang
Department of Chemistry
Functional Materials
Technische Universität Berlin
Hardenbergstraße 40, 10623 Berlin, Germany

M. Exner
Institut für Chemie
Humboldt-Universität zu Berlin
Brook-Taylor-Str. 2, 12489 Berlin, Germany

is critical to investigate the structure and chemistry of cells over multiple length scales, from nanoscale to electrode level, from coin cells to prototype pouch cells, to identify dominant reasons for poor performances, including low capacity, rapid degradation, and cell failure of practical Li-S pouch cells.[8,9,12,13]

As it is known, realizing lean-electrolyte operation (with an electrolyte/sulfur (E/S) ratio below 5 μL mg^{-1}) is one of the most crucial primary critical metrics for achieving high-energy-density prototype Li-S pouch cells.[8–10,14] However, lean electrolyte results in more severe cell degradation or cell failure compared to electrolyte-rich conditions.[8,15–17] Concerning that electrochemical reactions mainly occur at electrode/electrolyte interfaces, electrolyte wetting, which determines the mass transport and charge transfer from the bulk liquid phase to interfaces, is crucial in Li−S batteries to ensure the efficient occurrence of electrochemistry and subsequent electrochemical/chemical reactions. Particularly, unlike in carbonate electrolytes in lithium-ion batteries, the conventional ether-based electrolyte participates extensively in the dissolution-precipitation conversion reactions [18,19] leading to activation of sluggish sulfur species and accelerating kinetics, which is extremely significant for cell operation.[19] Thus, under lean-electrolyte conditions, poor quality of electrolyte wetting on electrodes and other components can easily cause cell failure.[15,19]

Therefore, critical questions raised are how electrolyte wets electrodes, infiltrates electrode pores, and distributes in the lean-electrolyte Li-S pouch cells, and then how these properties affect cell performance. Because of the closed configuration of batteries, it is extremely challenging to observe the quality of electrolyte wetting non-destructively. Although X-ray tomography has been reported to examine electrode structures of batteries and sulfur distribution in Li-S batteries,[20–22] it is not sensitive to most of the liquid electrolytes and therefore cannot be easily used to directly visualize electrolytes in batteries, including the Li-S system. Previously, fresh and not sufficiently reacted sulfur cathodes and Li anodes were observed after long cycling by only *ex situ* measurements [15] indicating that the electrolyte was not homogeneously distributed in the Li-S pouch cells under lean-electrolyte conditions. The poor wetting caused uneven reaction between sulfur and lithium, and the aggravated degradation of pouch cells. Based on simulations of electrolyte infiltration in electrodes, electrolyte deficiency is understood to originate from electrodes center and then spread to the edges.[15] Recently, Strubel et al. employed physisorption methods to analyze textural transformations and found that the electrolyte with high polysulfide solubility can lead to extreme redistributions of active materials, implying the heterogeneity of electrolyte distribution.[23] The redistribution of sulfur-based active materials has been visualized by X-ray tomography, revealing the dissolution of polysulfides from cathodes to the bulk electrolyte and the precipitation of lithium sulfides.[20,21,24] These remarkable works indicate the correlation between the redistribution of sulfur and electrolyte, but still lack the firsthand information from the electrolyte side. Upon that, the dynamic electrolyte wetting, infiltration, and distribution, and their effects on cell performances and degradations in the Li-S systems are anyway still elusive because of lacking *operando/in situ* techniques that can directly and non-destructively visualize electrolyte in the original and under charging/discharging cell conditions.[10,25]

Neutron imaging can be a powerful technique for visualizing electrolytes inside batteries non-destructively, as hydrogen atoms strongly scatter neutrons.[26–31] The spatial resolution of neutron tomography is lower than the complementary X-ray techniques (due to the electro-neutrality of the neutron requiring a stage detection process – conversion + scintillation), but neutrons are more penetrative and very meaningful to inspect the distribution of the Li-rich electrolyte over the entire area of the pouch cell.[32] Previously, neutron imaging was employed for studying electrolyte filling and wetting processes in lithium-ion pouch cells, showing a 2D distribution of electrolyte in cells.[33] Through neutron imaging, the electrolyte filling process in lithium-ion batteries (LIBs) was visualized, demonstrating that cells adsorbed electrolyte more quickly in a vacuum than under ambient pressure conditions, and the wetting process took place from the periphery to the center in a similar fashion. In addition, Michalak et al. directly observed out-gassing processes caused by oxidation and reduction of electrolyte solvent in LIBs through in situ neutron imaging.[34] But for a practical multi-layer Li-S pouch cell, *in situ/operando* neutron tomography has not been presented so far for the analysis of electrolyte distribution. The real-time evolution of electrolyte in different layers of Li-S pouch cells during charge and discharge has not been revealed either. In comparison with LIBs, the complicated electrochemistry and chemistry involved with electrolyte at interfaces in Li-S systems remain elusive and challenging for *operando*/in situ analysis, without saying the immature commercialization of the technology. Additionally, the practical lean electrolyte condition suffers from more severe electrolyte deterioration and consumption due to polysulfide dissolution, which differs from electrolyte changes in LIBs, which makes the analysis more challenging.

In this work, *operando* neutron imaging with a spatial resolution of ≈50 μm was explored to visualize the electrolyte distribution in Li-S pouch cells non-destructively. The two-layer Li-S pouch cells meet key practical parameters with high sulfur content (80 wt.% of sulfur in electrode materials), high sulfur loading (≈5 mg cm^{-2}), and lean electrolyte (E/S ≈5 μL mg^{-1}). By *operando* neutron tomograms, we visualized and imaged the dynamic distribution of electrolyte in different layers under various cell conditions including rest and battery cycling at different current densities. Impressively, it was found that the cell charge and discharge can promote the wetting and enable the activation of active materials, meanwhile leading to the electrolyte redistribution processes with "breath-in" and "breath-out" periodical behaviors. The evolution of electrolyte redistribution has been found to be correlated to the electrochemistry and chemistry processes, where the formation and dissolution of polysulfides in the electrolyte are mainly involved. The results also provide a deep understanding of the degradation mechanisms of Li-S pouch cells caused by the heterogeneous electrolyte distribution.

Y. Lu
Institute for Technical and Environmental Chemistry
Friedrich-Schiller-Universität Jena
Philosophenweg 7b, 07743 Jena, Germany
Y. Lu
Helmholtz Institute for Polymers in Energy Applications (HIPOLE Jena)
Lessingstraße 12, 07743 Jena, Germany

Our *operando* neutron tomography results not only provide direct dynamic observations of electrolyte distribution and redistribution in Li-S batteries and offer new insights into the failure mechanisms of practical Li-S pouch cells, but also are beneficial for rational design of metal-sulfur batteries to overcome the poor wetting issues.

2. Results and Discussion

2.1. *Operando* Neutron Imaging of Electrolyte Distribution

The neutron imaging of the electrolyte is non-destructively obtained based on mapping the transmission of the neutron beam. Some light atoms, such as hydrogen and lithium, mainly from solvents and salts of the ether electrolyte, exhibit relatively higher attenuation coefficients than heavier atoms (**Figure 1**a,b).[27,28] Importantly, *operando* neutron imaging can be achieved with the designed setup, where the cells can be discharged and charged controlled by a potentiostat (schematically illustrated in Figure 1b and Figure S1, Supporting Information). For approaching practical parameters, the electrode material consisted of 80 wt.% of sulfur with an areal loading reaching 5 mg cm^{-2}, and the electrolyte was at a lean amount (E/S≈5 µL mg^{-1} of sulfur). In addition, visualization of electrolyte from different layers of multilayer pouch cells is meaningful for studying the details of local electrochemical behaviors for practical pouch cells. The *operando* setup enables this function by rotation of pouch cells over 360° during wetting and discharge/charge, allowing the neutron beam passing through the cells from different angles. The reconstruction of the 3D matrix of attenuation coefficients from the 2D angular projections by applying a tomography approach represents the spatial distribution of the electrolyte from different layers of the cells in the cell volume. To validate it, the pouch cells were designed with two layers of single-sided sulfur cathodes and one layer of double-side lithium anode (Figure 1c).

Probing ether electrolyte distribution in Li-S batteries by neutron tomography is validated, and the correlations between the electrolyte distribution and the electrode properties have been first investigated. **Figure 2**a,c show the neutron tomograms of the cycled Li-S pouch cells for different layers. The inhomogeneous patterns with different contrast were observed, which originate from neutron interactions with nonuniformly distributed electrolyte. Especially, the dark areas because of the neutron attenuation showing roughly round shapes (e.g., marked with red arrows) and different sizes ranging from sub-mm to several centimeters are randomly distributed in the images, indicating the insufficient wetting (named by unwetted) region. Meanwhile, the other relatively bright areas (e.g., marked with green circles) related to high intensity of neutron attenuation are for sufficiently wetted regions (named as wetted regions). To evaluate the effects of nonuniform distribution of electrolyte on electrode reactions, the cycled Li-S pouch cells after *operando* measurements were disassembled. The optical profiles for both cathodes (Figure S2, Supporting Information) and anodes (Figure 2b,d) showed similar patterns as the neutron tomograms (Figure 2a,c). This indicates that wettability is relevant to both the electrolyte–lithium metal interface and the electrolyte–sulfur cathode interface. Specifically, the anodes show two differently colored regions, where a silver-like metallic color and a grey/black appearance can be distinguished. The former indicates that the portion of lithium anodes does not deeply react (or fresh) due to lacking electrolyte, while the latter corresponds to heavily reacted lithium with electrolyte after discharge and charge. To inspect the differences in surface microstructures, scanning electron microscopy (SEM) measurements were performed for the metallic-color areas (named as unwetted area) and grey areas (named as wetted area) of the cycled lithium anodes. The metallic-color areas exhibited a very dense and flat surface similar to the fresh lithium foil (Figure 2e top), while the grey areas displayed a highly porous and pulverized structure (Figure 2e bottom), which can be caused by the repeated lithium plating and stripping. X-ray photoelectron spectroscopy (XPS) was carried out to detect the surface chemical states of key elements on the cycled lithium anode. As shown in Figure S3 (Supporting Information), the XPS spectra of Li1s for unwetted and wetted lithium anode indicate that the wetted surface of cycled lithium anode exhibits more Li-O, Li-S_n, and Li-SO_x than the unwetted surface. As these lithium chemical states mainly originated from the solid electrolyte interphase (SEI) film, it revealed that better wetting results in more electrolyte reacting with lithium and leads to form more SEI during Li stripping/deposition.[25] Meanwhile, only a slight amount of bridging sulfur atoms (S_B) and terminal sulfur atoms (S_T) from lithium polysulfides existed in the unwetted region of the lithium anode, but S_B and S_T displayed a much higher intensity in the wetted region of lithium anode.[35] The XPS results supported that the unwetted area contained relatively fresh lithium or a very thin oxidized surface. The wetted area of the lithium anode presented a rough and cracked layer containing SEI debris and possibly cycled dead-Li on the anode surface (presence of Li^0). The above results show that the neutron imaging technology is able to observe the electrolyte distribution of Li-S pouch cells non-destructively, and the results revealed the correlation between the chemical states of electrodes (particularly for Li-metal anodes) and the electrolyte wetting.

2.2. Dynamic Electrolyte Wetting During Cell Rest and Redistribution During Cycling

O*perando* neutron tomography was then performed to investigate the wetting and distribution of electrolyte in different layers of Li-S pouch cells under different cell states, which were selected as cell rest under open-circuit conditions, and galvanostatic charge and discharge at various current densities, respectively.

The neutron tomograms of electrolyte distribution in layer 1 for 6 h from the onset of imaging (marked as 0 h) are shown in **Figures 3** and S4 (Supporting Information). It should be pointed out that the period from the onset of electrolyte injection to the start of neutron tomography measurements (roughly half an hour) was not measured due to the transfer of cells to the setup and preparation, and the start of the measurements. As a result, a relatively large area of electrolyte distribution in the cell can be observed even at 0 h, and much electrolyte is accumulated in the edge areas. Similar patterns appeared that unwetted regions and wetted regions can be observed, which is consistent with Figure 2. It confirms that the poor wetting status and rather limited electrode-electrolyte interfaces are mainly caused by the heterogeneous distribution of electrolyte in the present practical

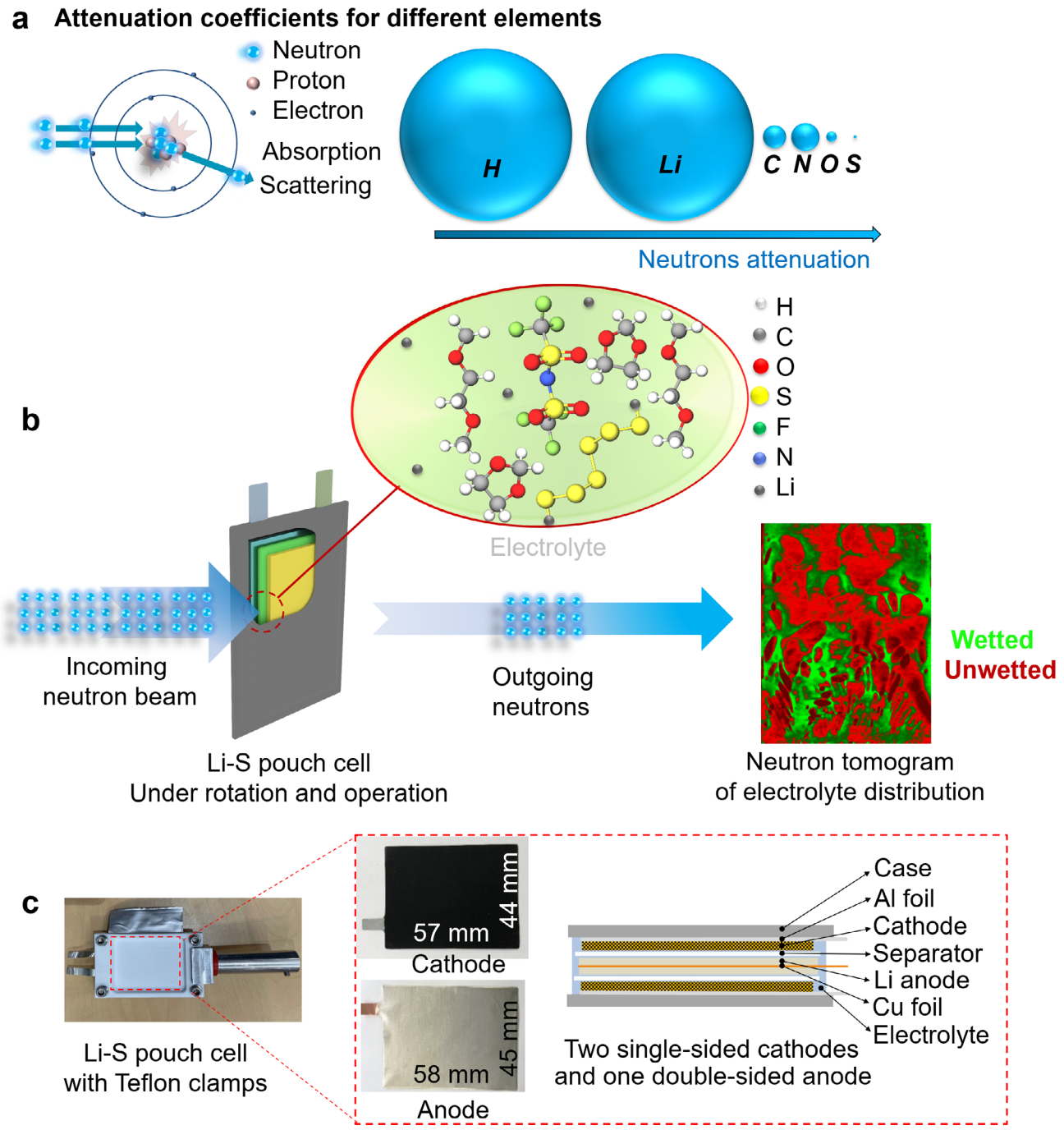

Figure 1. a) Schematic diagram of the interactions between neutrons and atoms, and the different attenuation coefficients for various main elements in the conventional ether-based Li-S electrolyte. The diameter of the spheres is proportional to the attenuation coefficients. b) Illustration of the imaging of the electrolyte when the neutron beam passing through a double-layer lithium-sulfur pouch cell. Green presents wetted regions; red, unwetted. c) The configuration of the studied pouch cell, containing two layers of single-sided cathode and one layer of double-side Li anode.

Li-S pouch cells under the lean electrolyte condition. With increasing the rest time, it can be clearly seen that the unwetted areas and shapes in some local regions changed, indicating the electrolyte redistributed (Figure 3 and Video S1, Supporting Information). Two typical behaviors can be noticed: the agglomeration and shrinking of unwetted areas. In the aqua-circle marked areas, these unwetted regions grew larger mostly by merging the neighboring unwetted areas. This process can be due to the movement and accumulation of bubbles between the voids of particles. Meanwhile, accompanied with the bubble flowing, some local boundaries (e.g., white-circle marked regions) diminished, and the isolated unwetted spots became smaller or disappeared (e.g., white marked regions), likely due to the electrolyte penetration driven by capillary forces. To be noticed, many merging

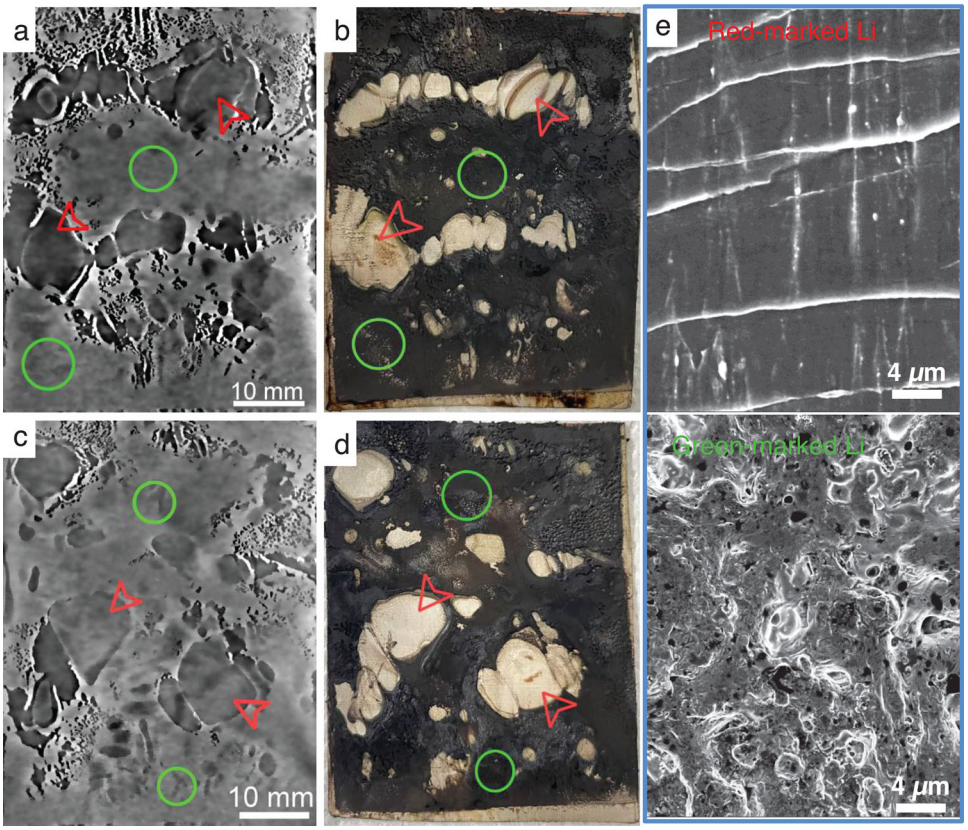

Figure 2. a,c) Vertical slice of the tomograms of the Li-S pouch cell after cycling for layer 1 and 2, respectively. Red arrows show the non-fully wetted regions, and green circles show the relatively fully wetted regions; b,d) optical photos of cycled anodes for layer 1 and layer 2, respectively. Red arrows and green circles show the same areas with marked tomograms in (a) and (c); e) SEM images of anodes from the Li-S pouch cell after neutron imaging measurements: top image is for red-arrow marked area with non-fully-wetted lithium anode (of layer 1), while bottom image is for green-circle marked area with fully-wetted lithium anode (of layer 1).

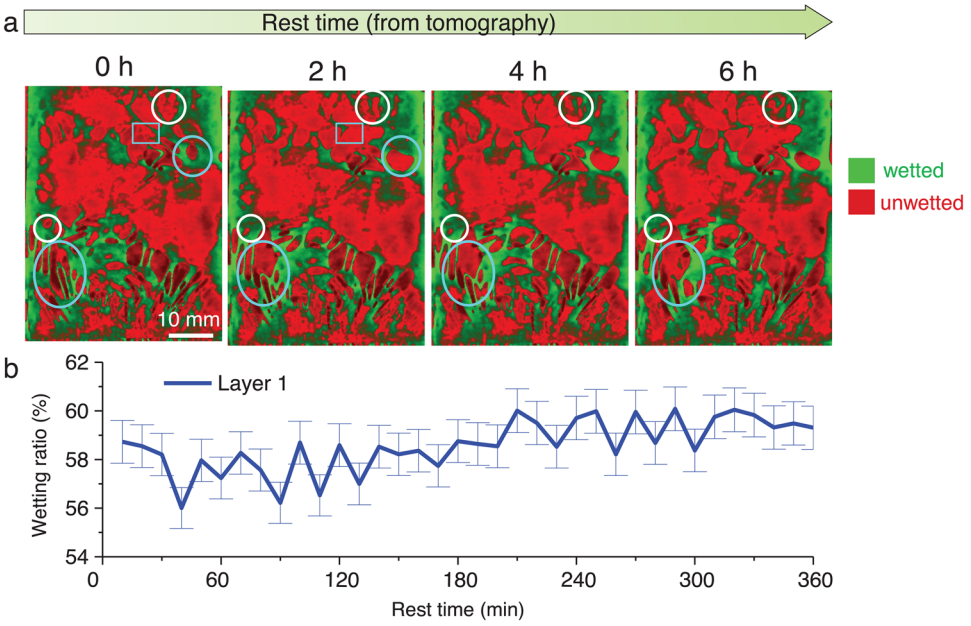

Figure 3. a) Vertical slices of the *operando* neutron tomograms of the Li-S pouch cell (layer 1) for wetting from 0, 2, 4 to 6 h. Marked aqua circles: locations for merged non-wetted regions; aqua rectangles: locations for disappeared boundaries; white circles: locations for diminished non-wetted regions and enlarged wetted regions. b) The quantitative curves of wetting ratio for layer 1 during rest.

events occurred in the early periods, such as within the initial 2 h under cell rest, while only slight changes of the unwetted shapes and areas were observed afterward (e.g., 4 – 6 h). This indicates that the wetting mainly occurs in the early period after the injection of electrolyte, while afterward only slow infiltration of electrolyte happens in the Li-S pouch cell under the lean electrolyte condition. Moreover, in layer 2, the electrolyte distribution and evolution during rest followed similar behaviors with those in layer 1, suggesting the consistent poor wetting of electrolyte in the multilayer Li-S pouch cells.

The dynamic wetting ratio (the ratio of wetted area to the overall area) was quantitatively analyzed for layer 1 (Figure 3b) and layer 2 (Figure S4, Supporting Information). In layer 1, the overall wetting ratio started at ≈58%, and increased slightly to ≈59% after 6 h of long-term rest, also accompanied with randomly low-amplitude fluctuations during the rest. The wetting ratio oscillations from Figure 3b and in Video S1 (Supporting Information) during cell rest at open-circuit potential (OCP) are primarily due to the statistical noise, limited temporal resolution, and electrolyte microflow movement during the tomography measurement. The above results further demonstrate that the long-term rest hardly improves the wetting heterogeneity under such lean-electrolyte conditions and electrode chemistries, but can only slightly alter the local wetting area, assumed to be produced by the movements of bubbles and electrolyte microflow. In layer 2, the initial wetting ratio was 64% higher than that in layer 1, mainly due to the electrolyte injection. After rest, the wetting gradually increased by a maximum ratio of 1%, which has a similar increment to layer 1.

After rest, the Li-S pouch cell was then galvanostatically discharged and charged at a relatively low current density of 0.06 C for 2 cycles, followed by 20 cycles at a higher rate of 0.3 C. This charge/discharge testing protocol was designed for the investigation of the effects of discharge-charge current densities on the electrolyte redistribution behaviors. It should be noted that the real current densities for the wetted reaction area were 0.1 C (for 0.06 C) and 0.5 C (for 0.3 C) when calculated based on the wetting ratio (59%), and varied with the changes in wetting. The initial capacity of the pouch cell at 0.06 C attained 410 mAh g^{-1}, but when normalized to the mass of the wetted electrode material (63% wetted area after 1st discharge), the actual capacity reached approximately up to 650 mAh g^{-1}. The above analyses suggest that the limited electrolyte–electrode interfacial area, primarily due to insufficient electrolyte wetting and the high local current density, are the main causes of the low capacity. Notably, under the critical practical conditions such as high sulfur loading (>5 mg cm^{-2}) and limited electrolyte (<5 µL mg^{-1}), achieving high capacity (e.g., >1000 mAh g^{-1}) with these commercial carbon materials is challenging unless surface treatments or catalysts are employed.

During discharge, the two sulfur reduction curves presented the typical sulfur redox behaviors consisting of two main electrochemical conversion processes, which are for solid sulfur to long-chain polysulfides and long-chain polysulfides to lithium disulfide/sulfide at the voltage plateaus of ≈2.0–2.4 and 1.7–2.0 V, respectively. In the charging process, the curves followed the reverse oxidation processes, which are the transformation of lithium sulfide/disulfide to long-chain polysulfides and then to sulfur. The gradual evolution of electrolyte redistribution during cycling can be clearly observed from Video S2 (Supporting Information). The quantitative analysis shown in **Figure 4b** presents in-depth results that show the obvious dynamic wetting ratio over the discharge and charge. To inspect more details on the dynamics, 12 key discharge/charge states were selected (Figure 4a), which are at the two typical reaction plateaus (e.g., at 2.1–2.4 and at ≈2.0 V) and at the ends of the charge (2.8 V) and discharge (1.7 V) of each cycle. As seen from Figure 4b, from the initial fresh cell to State 2 with depth of discharge (DOD) to ≈2.0 V, the electrolyte wetting ratio gradually increased from 59.5% to 64.0% (by 4.5%), which is a significantly increased fraction in comparison to the improvement observed by rest conditions. Then, from State 2 to State 3 (DOD 1.7 V), the electrolyte wetting ratio seemed to be kept constant or only slightly decreased. The oberved impressive evolution of the electrolyte wetting can be assumed to be caused by the underlying electrochemical and chemical reaction processes. Specifically, the sulfur conversion from fresh cell to State 2 corresponds to the following reaction I:

$$S_8\,(s) + Li \rightarrow Li_2S_x\,(l)\ (x = 4 - 8) \quad (1)$$

where solid sulfur was electrochemically converted to long-chain polysulfides (Li_2S_8, Li_2S_6 and Li_2S_4) as confirmed by *operando* Raman analysis (Figure S5, Supporting Information).[36,37] After that, they were solvated and dissolved in the electrolyte with fast kinetics.[9,38] The electrochemical processes and fast kinetics can be revealed by distribution of relaxation times (DRT) analysis (Figure S6, Supporting Information) from *operando* electrochemical impedance spectroscopy (EIS) analysis.[39,40] During this process, electrolyte was "breathed in", leading to increased electrolyte-electrode interfaces and improved wetting ratio. Then, reaction II below expressed the sulfur redox conversion from State 2 to State 3:

$$Li_2S_x\,(l) + Li \rightarrow Li_2S_y\,(s)\ \ (y = 1 - 3) \quad (2)$$

where long-chain soluble polysulfides were electrochemically reduced to less-soluble short-chain polysulfides (e.g., Li_2S_2) or insoluble lithium sulfides.[38,41] The process encounters the desolvation and precipitation reactions, resulting in the release and accumulation of electrolyte at local interfaces and causing the slightly decreased wetting ratio (by ≈1.0%). Meanwhile, charge transfer resistance and diffusion resistance increased due to the precipitation reactions (Figure S6, Supporting Information). In the following charge process from State 3 to State 5 (state of charge (SOC) to ≈2.4 V), the wetting ratio increased by an increment of 3%, which is presumed due to the reverse processes of II:[38,41]

$$Li_2S_y\,(s) \rightarrow Li_2S_x\,(l) + Li \quad (3)$$

where the insoluble lithium sulfide/less-soluble short-chain polysulfides were converted to high-soluble long-chain polysulfides by solvation, as unveiled by Raman analysis shown in Figure S5, Supporting Information), enabling "breath in" of electrolyte and improved wetting. As a result, the mass transfer became faster (Figure S6, Supporting Information). Finally, the transformation

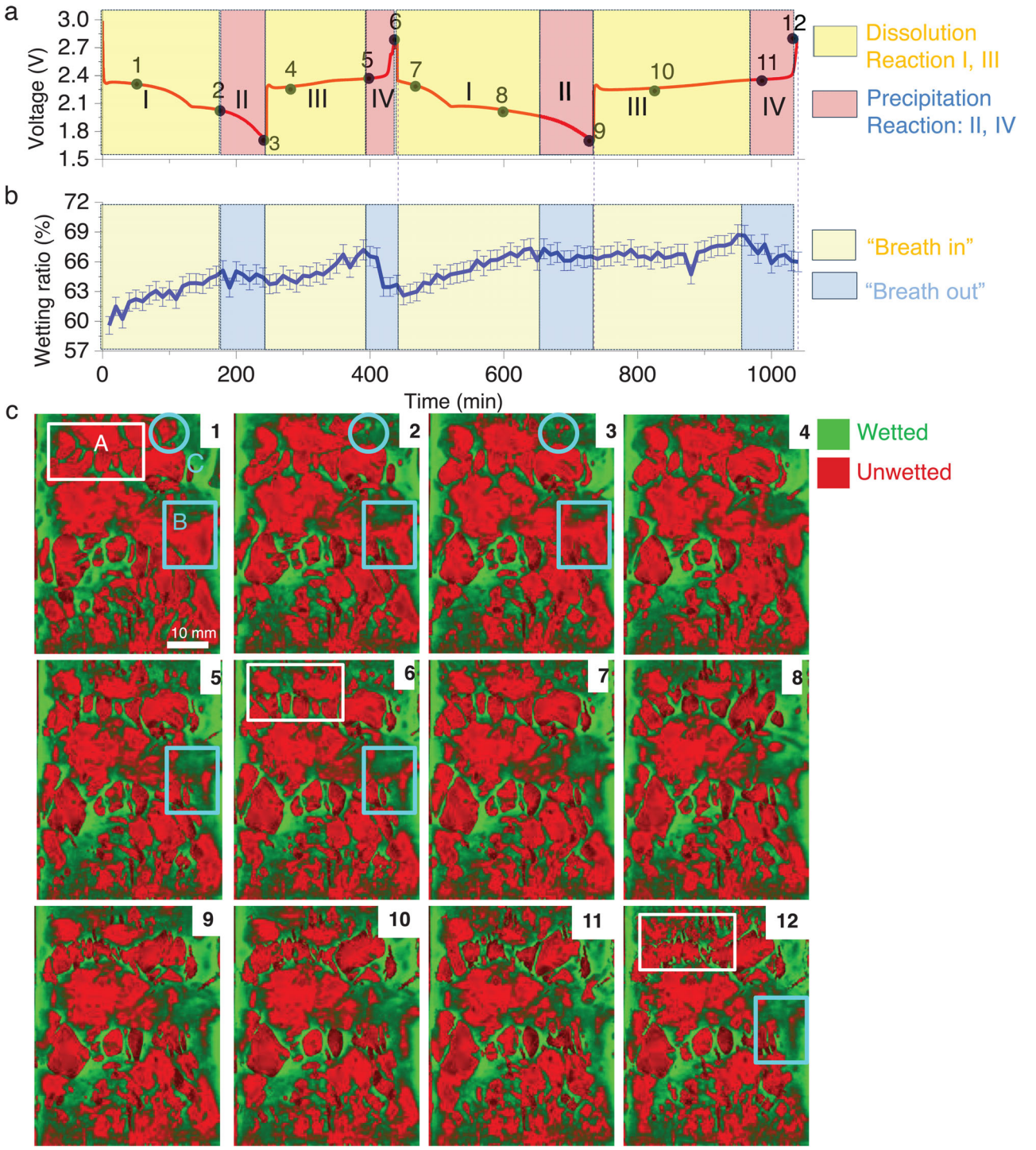

Figure 4. a) Charge and discharge curves of the Li-S pouch cell (layer 1) at 0.06 C; b) the quantitative curves of wetting ratio for layer 1 during battery discharge and charge. The marked colors present the processes of solvation and desolvation; c) *operando* neutron tomograms of key states for layer 1 during the discharge and charge of the Li-S pouch cell at 0.06 C.

from State 5 to State 6 (SOC 2.8 V) was a reverse reaction of I,[38,41,42]

$$Li_2S_x\,(l) \rightarrow S_8\,(s) + Li \quad (4)$$

which was accompanied with the desolvation of polysulfides and precipitation of solid sulfur, originating "breath out" of the electrolyte and ≈3% decrease of wetting ratio.

More interestingly, the evolution behaviour observed from the first cycle was periodically presented in the subsequent

charge/discharge processes, strongly indicating the correlation between dynamic electrolyte redistribution and the four types of sulfur redox conversions. Compared to the wetting ratio oscillations during cell rest, the breathing behavior differs significantly in both timescales (10 min vs ≈200 min) and amplitude (1-2% vs up to 5%) (Figure S7, Supporting Information). The "breath-in" and "breath-out" behaviours of electrolyte wetting during discharge and charge, to the best of our knowledge, were first observed in the Li-S batteries. This special behaviour was not assumed to be caused by the volume expansion of cathodes or cells, because no constant increase of electrolyte wetting during discharge from State 2 to State 3 was observed. Therefore, the "breath-in" and "breath-out" behaviours of the electrolyte with cell discharge/charge could be the special feature for the metal-sulfur batteries due to their dissolution-precipitation conversion processes. By *operando* neutron tomography analysis, we quantitatively revealed that the formation and solvation of soluble long-chain polysulfides during discharge and charge are the key to promoting the electrolyte wetting and redistribution in Li-S batteries.

Moreover, it can be seen that the improvement of electrolyte wetting dominantly took place in the 1st cycle (≈8% versus ≈6% for the 2nd cycle), leading to a significant increase of electrolyte-electrode interfaces. As a result, the charge/discharge time in the second cycle, as shown in Figure 4a, is considerably longer than those in the first cycle, indicating that more active materials at interfaces became wetted and activated, and the electrolyte redistribution induced enhanced homogeneity of the spatial sulfur distribution. These results agree with the X-ray tomography studies on sulfur redistribution during discharge and charge in Li-S systems.[20,21,24,43] Our neutron tomography findings reveal the important behavior and function of the electrolyte, which could mitigate the spatial heterogeneity of polysulfides and electrolyte in the electrodes and mediate the sulfur phase variation by the dissolution-precipitation conversion. The benefit of the improved wetting was indicated by the higher charge and discharge capacity in the second cycle than that in the first cycle (Figure S8, Supporting Information). This could well explain the reasons for the previously reported abnormal capacity increase,[42,11,44,45] known as the activation process of Li-S batteries in the initial numbers of cycling.

More details on electrolyte redistribution were examined from the tomograms selected from 12 key states (Figure 4c). The yellow-circle marked areas (region C) in States 1 to 3 corresponded to the 1st discharge induced homogeneity of electrolyte spatial redistribution, where the marked unwetted area diminished and nearly disappeared. This diminishment of electrolyte variation corresponded to the dissolution by reaction I. Despite an obvious transformation of the unwetted state to the wetted state, many unwetted areas (e.g., region A) suffered from shrinkage in the 1st discharge, but slightly. Nevertheless, a relatively large unwetted area in the same area turned into wetted after the subsequent charging process (region A and B from State 1 to 6). This evolution mainly took place from State 4 to 5, corresponding to reaction III: the conversion of short-chain polysulfides to long-chain polysulfides. The "breath-in and breath-out" behaviors of electrolyte wetting can also be clearly observed from tomograms, such as the wetting evolution from States 1 to 2 and 3 in region B. The inconspicuous or disappeared "breath-in" and "breath-out" behaviors in the same region from State 7 to 12 imply the local irreversibility: "breath-in" electrolyte > "breath-out" electrolyte. These evolution behaviors of electrolyte wetting are consistent with the quantitative analysis. As a result, the overall wetting ratio demonstrated a ≈6.1% increase after two cycles of discharge and charge at 0.06 C.

After initial discharge and charge at 0.06 C, the cells were followed by 20 cycles at a higher rate of 0.3 C. The dynamic evolution of electrolyte redistribution can be seen from Video S2 (Supporting Information). The galvanostatic discharge and charge curve in **Figure 5a** showed higher polarization at such current densities than that at 0.06 C, resulting in shorter time for charge output/input and smaller capacity (Figure S8, Supporting Information). Despite the high polarization, the two-voltage-plateau sulfur redox conversions are still present in the discharge. Figure 5b presents the corresponding quantitative analysis of dynamic electrolyte wetting with the discharge-charge operation. Consistent with observations at 0.06 C, electrolyte redistribution demonstrated electrolyte "breath-in" and "breath-out" behaviors from the 3rd cycle, which then repeated periodically with discharge and charge to the 6th cycle. Meanwhile, electrolyte "breath in" was closely correlated to the dissolution processes, reaction I and III, while "breath out" for the precipitation processes, reaction II and IV. Nevertheless, the amplitudes for "breath in" and "breath out" of electrolyte were relatively smaller due to the sluggish kinetics in comparison with cycling at 0.06 C. Additionally, after 10 cycles the overall average wetting decreased by 1.7%, which was presumed to be caused by the fast electrolyte consumption at such an increased charging rate.

To inspect more details of electrolyte redistribution, six key states, the beginnings and the ends for the 1st, 2nd, and 10th cycle were marked and selected shown in Figure 5a. 6 tomograms for these 6 key states were analyzed and compared to demonstrate the electrolyte evolution (Figure 5c). Different from Figure 4c, almost no large unwetted area with a few centimeters turned into wetted during cycling at 0.3 C. Instead, only small millimeter-sized unwetted areas evolved from bulk into granules (yellow marked region B). More detailed local evolution can be observed in the enlarged areas (of region A) shown in Figure 5d. The narrow and small portions of unwetted areas were gradually changed into smaller granules, hinting at the improvements of electrolyte spatial distribution. Detailed comparison of the electrolyte redistribution between slow and fast cycling can also be seen from Video S2 (Supporting Information).

For layer 2 under discharge and charge at 0.06 and 0.3 C, the dynamic electrolyte redistribution and selected tomograms of electrolyte distribution are shown in Figures S9,S10 (Supporting Information). The "breath-in" and "breath-out" behaviors of electrolyte redistribution under slow and fast discharge/charge can be also observed, which are similar to the observations in layer 1. This suggests consistent electrolyte redistribution occurring in the multilayer Li-S pouch cells. The above results also demonstrate that a lower current density is more beneficial for the activation of the Li-S multilayer pouch cell, as it enables homogeneous redistribution of the lean electrolyte than higher current densities, explaining the importance of employing testing protocols consisting of low current densities for activation of the Li-S cells to the greatest extent.

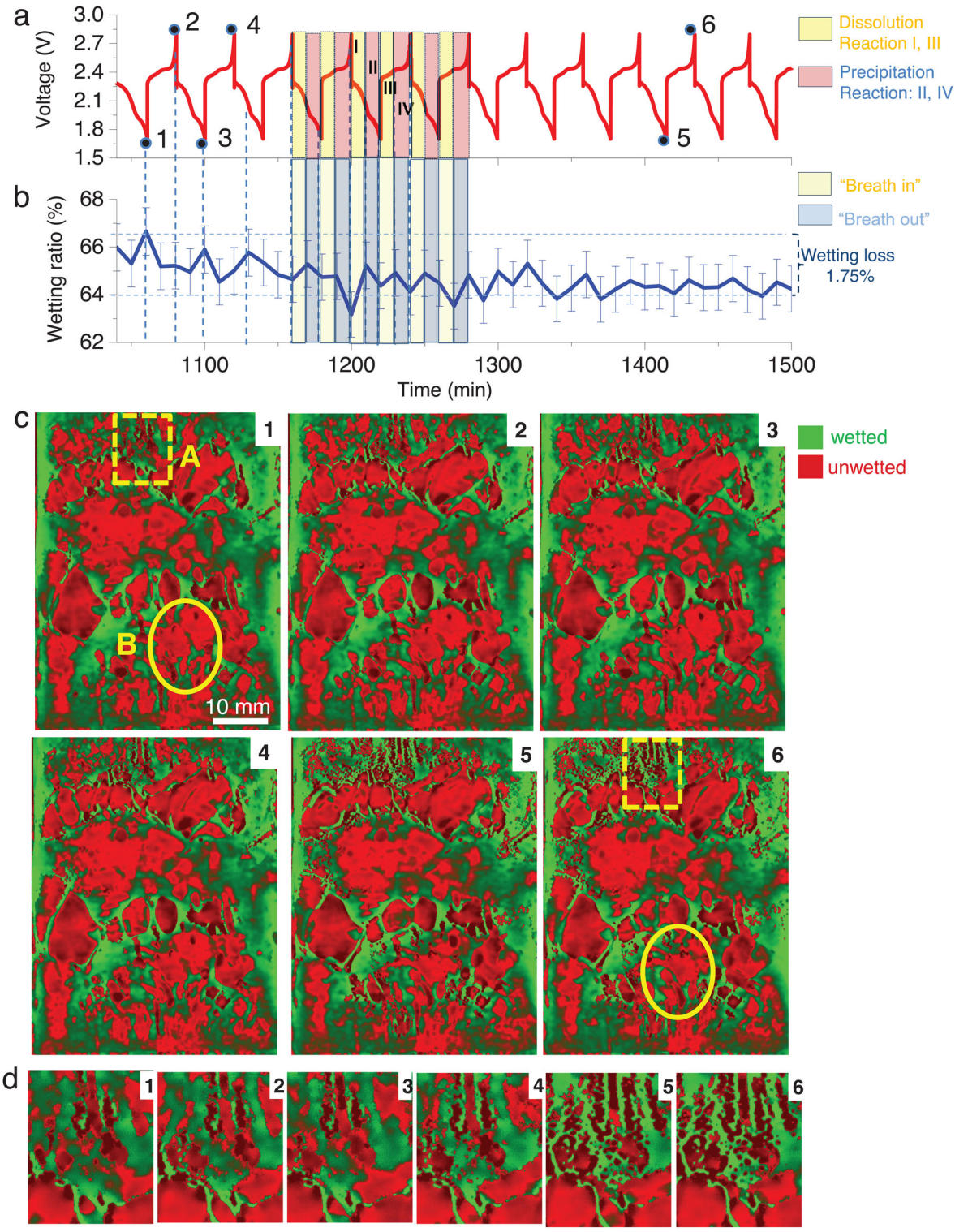

Figure 5. a) Charge and discharge curves of the Li-S pouch cell (layer 1) at 0.3 C; b) the quantitative curves of wetting ratio for layer 1 during battery discharge and charge; c) *Operando* tomograms of 6 key states for layer 1 in the Li-S pouch cell when discharged and charged at 0.3 C; d) magnified locations in the enlarged area of region A during cycling.

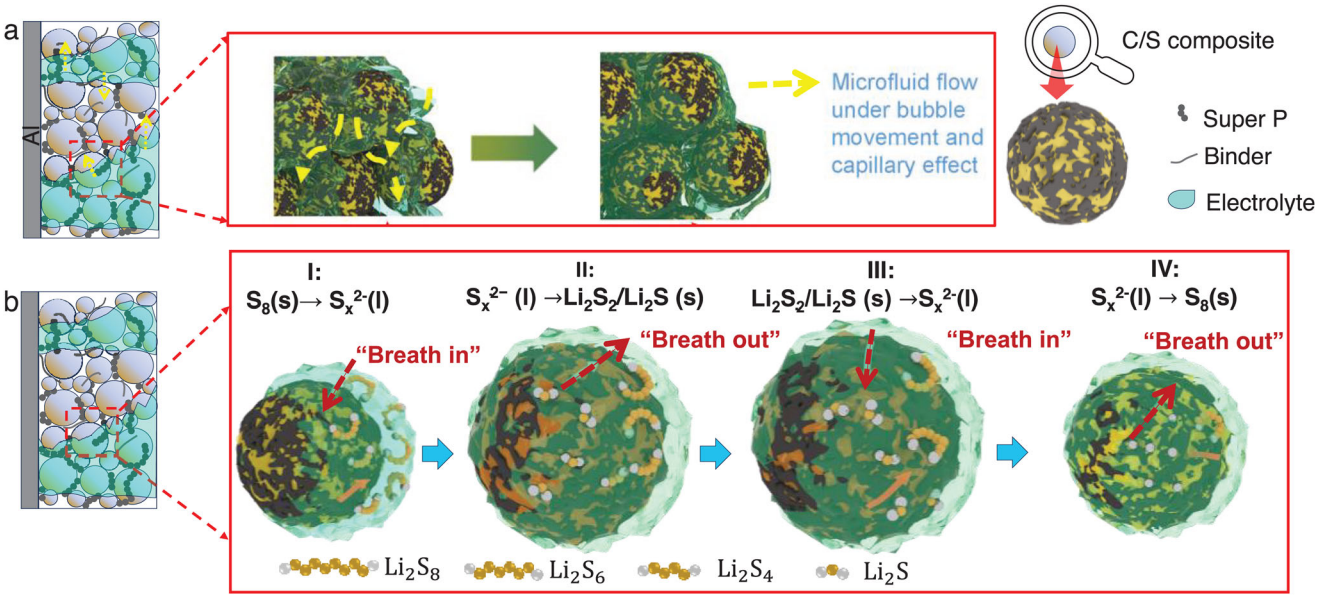

Figure 6. Schematic illustration of the evolution of electrolyte distribution and redistribution and electrolyte behaviors under different conditions: a) rest and b) discharge/charge. In figure b, the change of wetting and electrolyte is due to the different electrochemical reactions and solvation/desolvation of various sulfur species.

2.3. Discussion on the Evolution of Electrolyte Distribution During Wetting and Cycling

Electrolyte filling during the manufacture of lithium-sulfur pouch cells consists of dispensing and filling/wetting.[46,47] Dispersing produces an accumulation of electrolyte, where the electrolyte is injected and is more sparse in the edges. Then, in the filling and wetting process, electrolyte penetrates into the cells, such as the pores of electrodes and separators, by capillary forces (Figure S11a, Supporting Information).[26] However, for practical Li-S pouch cells, lean electrolyte conditions generate a greater variance of electrolyte distribution, resulting in inhomogeneous wetting and failing to wet the cells thoroughly (Figure S11b, Supporting Information). This leads to the low utilization of active materials, low capacities, and short cyclic life. Generally, battery rest or formation treatment can improve the wetting property by capillary forces and concentration gradient to mitigate the variation of electrolyte distribution. The observed merger of unwetted areas accompanied by boundary migration and diminishment is a result of the local movement of gases and electrolyte microfluids (**Figure 6a**). In our results, ≈1% increase in wetting was examined by neutron tomography. It confirms that long-term rest has little contribution to electrolyte wetting of Li-S pouch cells, which may be due to the poor electrolyte wettability on electrode materials and can be different from electrolyte wetting during rest in Li-ion batteries.[26,33,48]

In addition, other factors such as dispensing/injection methods, vacuum pressure, poor wettability of electrolyte on electrodes, and cell porosity also alter the wetting properties.[46,49,50] In our study, high capacity (987 mAh g^{-1}) was achieved with pouch cells containing similar E/S ratio of 5 µL mg^{-1} and sealed under a high vacuum pressure −25 kPa (Figure S12, Supporting Information). The improvement highlights the importance of electrolyte wetting in sulfur conversion. Meanwhile, it indicates that the poor wetting in lean-electrolyte Li-S batteries becomes one of the dominant reasons for the battery failure and rapid degradation.

Nevertheless, the improvement of wetting by rest treatment not only depends on rest time, but also relies on cell properties such as the wettability of electrolyte on electrodes and separators, and cell porosity.[49,50] The ketjen black-based cathodes, having high specific surface area, high pore volume, high tortuous and mostly mesoporous structures, make the electrolyte penetration more problematic compared with other low-specific-surface-area carbon materials such as Super P and carbon nanotubes. In addition, polar surfaces provide better wettability of electrolyte than ketjen black carbon, which is conducive to uniform wetting.

Subsequently, during battery discharge and charge, lithium ions (Li^+) and electrolyte molecules coordinate with electrochemically generated polysulfides by $S \rightarrow S_x^{2-}$ (e.g., x = 4 – 8) of reaction I in the discharging and $Li_2S/Li_2S_2 \rightarrow S_x^{2-}$ (e.g., x = 4 – 8) of reaction III in the charging (Figure 6b),[41] forming solvated complexes stabilized by solvation shells of 1, 3-dioxolane (DOL) and 1, 2-dimethoxyethane (DME) from the ether-based electrolyte.[51–53] The high solubility of long-chain polysulfides (e.g., Li_2S_8, with a solubility of ≈6600 mM based on sulfur atom) in the ether electrolyte (1 M LiTFSI in DOL/DME) drives the formation of high-concentration solvated complexes stabilized by DOL/DME coordination in their solvation shells, which "breathes in" electrolyte and promotes the wetting, meanwhile leading to activation of more "isolated" active materials for participating into the subsequent electrochemical/chemical conversions.[19] The catalytic function of polysulfides, or being as a "healing agent" in Li-S batteries for activation of "isolated" sulfur, has been reported previously.[54] Thus, the observed electrolyte redistribution by *operando* neutron tomography can be correlated to the formation of solvated structures. These processes can be reversible but not entirely, due to the desolvation and reduction of the solubility of

some sulfur species during the phase conversions, resulting in the observation of less "breathing out" of electrolyte (Figure 6b).

Other noteworthy points are: 1) the *operando* neutron tomography results emphasize the significance of ether electrolyte in the Li-S or metal-sulfur battery systems. Previously, X-ray tomography revealed the redistribution of sulfur in the ether-electrolyte Li-S system.[20,21,24] However, these works could not provide the original information about the role and behaviors of the electrolyte. The neutron imaging results in this study, in combination with the electrochemical behaviors, instead provide this first-hand information. The coherent findings on the re-distribution of electrolyte from neutron tomography and the re-distribution of active sulfur species from X-ray tomography and physisorption methods offer a comprehensive understanding of the spatial redistribution of active materials by solvated structures containing DOL and DME molecules, thus providing new insights into these evolution dynamics. It also implies the properties of electrolytes, such as the solubility of polysulfides could alter the electrolyte wetting behaviors supposing no dissolution-precipitation conversions, but solid-solid conversions only occur. 2) As the dissolution of long-chain polysulfides is rate-limited for the high-sulfur-loading cathodes under such lean electrolyte conditions, *C*-rate notably influences the wetting and redistribution of electrolyte. Two battery cycles of discharge and charge at 0.06 C led to 7% wetting increase overall, which is markedly higher than rest or higher-rate cycling. The dominant reasons are supposed to be reactions I and III, rather than reaction II, which means the sluggish kinetics for reaction II at higher rates do not work much on the wetting improvement. 3) Under lean electrolyte conditions, more cycling could result in poorer electrolyte wetting caused by electrolyte consumption, resulting in faster cell degradation. The phenomenon is more prominent under the higher-rate cycling as it easily induces new SEI formation, dendrite growth, and more rapid electrolyte depletion.[55,56] In addition, the deteriorated properties of the electrolyte such as increased viscosity and unfavorable wetting properties because of dissolved high-concentration polysulfides, can also reduce the wetting.[50] 4) The as-found cycling-dependence and influences of *C*-rates on wetting of electrolyte in Li-S batteries can be extraordinarily distinct from the Li-ion batteries due to the unique dissolution-precipitation reactions in the ether-based Li-S batteries.[26,28,48,57] These results are thus believed to be applicable to other metal-sulfur batteries with similar conversion processes. 5) Unveiling the correlation between wettability and electrode-electrolyte interfaces is essential to improve wettability in Li-S cells. Although wettability is relevant to both the electrolyte–lithium metal interface and the electrolyte–sulfur cathode interface, the dynamic changes in wettability during cycling are primarily associated with the polysulfide dissolution and precipitation reactions, which occur at the electrolyte–sulfur cathode interface. The primary factor influencing wetting at the electrode/electrolyte interfaces is the difference in electrode microstructure and surface properties. Lithium metal anode has a flat surface, while sulfur cathode features a porous structure with a high surface area that acts as an electrolyte reservoir. As a result, wetting at the electrolyte–cathode interface dominant and meanwhile guides electrolyte diffusion toward the anode, leading to matched optical profiles between the cathode and anode (Figure 2 and Figure S2, Supporting Information). In this case, rationally engineering cathodes could effectively improve the wettability of Li-S batteries.

3. Conclusion

For the first time, we presented *operando* neutron tomography for visualizing the electrolyte in multilayer Li-S pouch cells and investigated the electrolyte redistribution during rest and cycling. The distribution of the electrolyte in different layers reveal the inhomogeneous reaction of electrodes in Li-S pouch cells under the lean electrolyte conditions, resulting in comparably low capacities for the pouch cells. Battery rest and cycling of cells influence the electrolyte redistribution in the pouch cells. During battery rest before cycling, a conglomeration of unwetted regions in local regions occurred mainly in the early stages, while subsequent long-term rest contributes only marginally to the overall wetting ratio. Impressively, slow charge/discharge can significantly promote the wetting ratio and redistribution of electrolyte and enable the activation of cells. The evolution of electrolyte redistribution during cycling can be correlated to the electrochemical/chemical reactions, and the formation and dissolution of long-chain polysulfides, which are identified as the key process for the electrolyte redistribution. Due to the solvation and desolvation of sulfur species, the "breath-in" and "breath-out" behaviors of electrolyte redistribution periodically took place during discharge and charge at low current densities. These findings provide solid evidence of the uneven distribution of electrolyte in the Li-S pouch cell, help establish guidelines to optimize the testing protocols, and promote the investigation on the failure mechanisms and design of practical Li-S batteries from the perspective of electrolyte wetting to accelerate the commercialization of Li-S batteries. The neutron tomography approach proposed above opens new a prospect for electrolyte inspection and given that the above research findings can be easily extended to other metal-sulfur systems.

4. Experimental Section

Preparation of Ketjen Black/Sulfur Cathodes: All chemicals were used as received. Ketjen black (KB, EC-600 JD) was mixed with sulfur powder (Alfa Aesar) in a weight ratio of 2: 8 using a planetary micro mill (PULVERISETTE 7, Fritsch) at a speed of 400 rpm for 30 min. Then the ketjen black/sulfur (KB/S) was put into poly(tetrafluoroethylene)-lined autoclaves, sealed in an Ar-filled glove box, and heated at 155 °C for 12 h. Slurry was formulated by ball-milling mixing of the as-obtained KB/S composite with Super P carbon black (Alfa Aesar), and sodium carboxymethyl cellulose (CMC, Alfa Aesar)/poly(styrene-cobutadiene) (SBR, Alfa Aesar) in a water and ethanol mixture solvent. The weight ratio of active material, Super P, and binder (CMC/SBR) was 8: 1: 1. Then, the slurry was both double-sided coated and one-side coated on a carbon-coated aluminum foil with an automatic film coater (MSK-AFA-II, MTI corp.). The cathodes were dried in air at room temperature for 5 h, followed with further drying at 60 °C. The cathode was then calendared to ≈100 µm using a rolling press (MSK-HRP, MTI corp.). The sulfur areal loading on a single side was ≈5 ± 0.5 mg cm^{-2}. Finally, the cathode was cut into pieces (57 mm × 44 mm) for pouch cell fabrication.

Assembly of Li-S Pouch Cells: Double-sided lithium coated on copper foil (100 µm in total) (China Energy Lithium Co., Ltd) was punched to pieces (58 mm × 45 mm) as the Li metal anodes. Two single-sided cathodes, a separator (Celgard 2400), and one double-sided anode were stacked together in a Z stacking method using a stacking

machine (MSK-111A-L, MTI corp.). The pouch cell without electrolyte was assembled and then sealed with a vacuum (-90 kPa) and a hot sealer (at 180 °C, MSK-115-III, MTI corp.). Then the electrolyte, 1 M lithium bis(trifluoromethanesulfonyl) imide (LiTFSI, Alfa Aesar) in 1, 3-dioxolane (DOL, Alfa Aesar) and 1, 2-dimethoxyethane (DME, Alfa Aesar) (1: 1, v/v) with 0.3 M $LiNO_3$, was injected into the pouch cell from a small hole on the edge of pouch cell. The injected amount of electrolyte was for an E/S ratio of ≈5 µL mg^{-1} of sulfur. The pouch cell was then sealed using a portable hot sealer (no vacuum). All the above cell assembly and electrolyte injection processes were performed in a glove box filled with argon with both oxygen and moisture levels below 0.1 ppm. The Li-S pouch cells were immediately transferred to the *operando* setup, installed, and measured via *operando* neutron imaging. The neutron imaging background of pouch cells before the addition of electrolyte was first removed.

Electrochemical Measurements: The fresh Li-S pouch cells were under rest (or aged) for 6 h, then the cells were galvanostatically cycled within the voltage window of 1.7–2.8 V at different C rates (1 C = 1675 mA g^{-1}). The initial two cycles were operated at 0.06 C, followed with twenty cycles of charge and discharge at 0.3 C. The electrochemical measurements were performed with a potentiostat of Gamry Instruments (Interface 1010E). The *operando* electrochemical impedance spectroscopy was measured with pouch cells by applying an amplitude voltage of 10 mV within 0.1–10^5 Hz, meanwhile, the pouch cells were under discharge and charge at 0.06 C for 2 cycles and 0.3 C for one cycle. The DRT fitting and interpretation were conducted following the methodology reported previously.[39]

Material Characterization: XPS measurements were carried out on a Thermo Scientific K-Alpha+ X-ray photoelectron spectrometer (ESCALab220i-XL) with Al Kα radiation. The samples were loaded onto a vacuum transfer holder inside an Argon glove box and then transferred into the spectrometer under vacuum. SEM measurements were performed on a scanning electron microscope (Zeiss Crossbeam 340) at room temperature. The samples were placed in a transfer shuttle in the argon-filled glove box and transferred into the scanning electron microscope to prevent oxidation by air. *Operando* Raman spectroscopy was conducted with the Renishaw InVia confocal Raman microscope with a 532 nm laser of 0.05% energy. *Operando* spectroscopy was performed using an EL-Cell ECC Opto-10 cell holder (as shown in Figure S5, Supporting Information), where a two-electrode face-to-face configuration featuring a sulfur electrode stripe and a metallic counter electrode was utilized. The cell was cycled at a rate of 0.06 C.

Operando Neutron Imaging: *Operando* neutron tomography experiments were performed at the neutron imaging instrument Neutron and X-ray Tomography (NeXT) at Institut Laue-Langevin (ILL). The used collimation ratio (L/D) of 600 with a sample/detector distance of 30 mm yielded a geometrical blurring of 50 µm. A pixel size of 26 µm was chosen, and the thickness of the scintillator screen (ZnS: ^{6}LiF) of 100 µm was well adapted to this image blur. The detector system was based on sCMOS camera Hamamatsu ORCA (2048×2048 pixels) viewing the scintillator through a mirror. The high neutron flux of ≈3 × 10^8 n cm^{-2} s^{-1} allowed for exposure time of 0.6 s per image which helped us to perform tomography scans with 1000 projections per 360° in 10 min.

Supporting Information

Supporting Information is available from the Wiley Online Library or from the author.

Acknowledgements

The authors acknowledge the Ni-Matters joint research unit for providing beam time at the NeXT instrument at ILL for performing of the neutron tomography investigation. K. Dong would like to acknowledge the Scientific and Technological Innovation project of Institute of High Energy Physics, Chinese Academy of Sciences (No. E4545CU2, No. E35451U2). Q. Wu acknowledges Alexander von Humboldt's research fellowship. Y. Lu thanks the support from the German Ministry of Education and Research (BMBF) within the research program Batterie 2020 (Förderkennzeichen: 03XP0398D, SkaLiS) and EU Horizon Europe project (GA101104006, HealingBat, part of BATTERY2030+).

Open access funding enabled and organized by Projekt DEAL.

Conflict of Interest

The authors declare no conflict of interest.

Data Availability Statement

The data that support the findings of this study are available from the corresponding author upon reasonable request.

Keywords

dynamic evolution, electrolyte wetting, lean-electrolyte pouch cells, Li-S batteries, operando neutron imaging

Received: March 9, 2025
Revised: July 8, 2025
Published online: August 7, 2025

[1] Z. W. Seh, Y. Sun, Q. Zhang, Y. Cui, *Chem. Soc. Rev.* **2016**, *45*, 5605.
[2] G. Zhou, H. Chen, Y. Cui, *Nat. Energy* **2022**, *7*, 312.
[3] Y. Xiang, L. Lu, A. G. P. Kottapalli, Y. Pei, *Carbon Energy* **2022**, *4*, 346.
[4] A. Bhargav, J. He, A. Gupta, A. Manthiram, *Joule* **2020**, *4*, 285.
[5] W. Ren, W. Ma, S. Zhang, B. Tang, *Energy Storage Mater.* **2019**, *23*, 707.
[6] D. Liu, C. Zhang, G. Zhou, W. Lv, G. Ling, L. Zhi, Q. H. Yang, *Adv. Sci.* **2018**, *5*, 1700270.
[7] D. Xie, Q. Wu, M. K. Elibol, L. Jiang, Y. Lu, *Curr. Opin. Green Sustain.* **2024**, *49*, 100958.
[8] Z. X. Chen, M. Zhao, L. P. Hou, X. Q. Zhang, B. Q. Li, J. Q. Huang, *Adv. Mater.* **2022**, *34*, 2201555.
[9] J. Chen, Y. Fu, J. Guo, *Adv. Mater.* **2024**, *36*, 2401263.
[10] S. Dörfler, H. Althues, P. Härtel, T. Abendroth, B. Schumm, S. Kaskel, *Joule* **2020**, *4*, 539.
[11] L. Qie, C. Zu, A. Manthiram, *Adv. Energy Mater.* **2016**, *6*, 1502459.
[12] S. Chen, C. Niu, H. Lee, Q. Li, L. Yu, W. Xu, J.-G. Zhang, E. J. Dufek, M. S. Whittingham, S. Meng, J. Xiao, J. Liu, *Joule* **2019**, *3*, 1094.
[13] S. Mei, Y. Xu, T. Quan, R. Garcia-Diez, M. Bär, P. Härtel, T. Abendroth, S. Dörfler, S. Kaskel, Y. Lu, *Batteries Supercaps* **2022**, *5*, 202100398.
[14] H. Pan, K. S. Han, M. H. Engelhard, R. Cao, J. Chen, J. G. Zhang, K. T. Mueller, Y. Shao, J. Liu, *Adv. Funct. Mater.* **2018**, *28*, 1707234.
[15] L. Shi, S.-M. Bak, Z. Shadike, C. Wang, C. Niu, P. Northrup, H. Lee, A. Y. Baranovskiy, C. S. Anderson, J. Qin, S. Feng, X. Ren, D. Liu, X.-Q. Yang, F. Gao, D. Lu, J. Xiao, J. Liu, *Energy Environ. Sci.* **2022**, *13*, 3620.
[16] H. Shi, W. Sun, J. Cao, S. Han, G. Lu, Z. A. Ghazi, X. Zhu, H. Lan, W. Lv, *Adv. Funct. Mater.* **2023**, *33*, 2306933.
[17] Q. Cheng, Z. X. Chen, X. Y. Li, C. X. Bi, F. Sun, X. Q. Zhang, X. Ma, B. Q. Li, J. Q. Huang, *Adv. Energy Mater.* **2023**, *13*, 2301770.
[18] G. Li, S. Wang, Y. Zhang, M. Li, Z. Chen, J. Lu, *Adv. Mater.* **2018**, *30*, 1705590.
[19] Y. E. Y. Liu, J. Meng, D. Aurbach, R. Zou, D. Xia, Q. Pang, *Joule* **2021**, *5*, 42.
[20] S. D. A. Matthew Sadd, S. Colding-Jørgensen, D. Blanchard, R. E. Johnsen, S. Sanna, E. Borisova, A. Matic, J. R. Bowen, *Adv. Energy Mater.* **2022**, *12*, 2103126.

[21] C. Tan, T. M. M. Heenan, R. F. Ziesche, S. R. Daemi, J. Hack, M. Maier, S. Marathe, C. Rau, D. J. L. Brett, P. R. Shearing, *ACS Appl. Energy Mater.* **2018**, *1*, 5090.
[22] M. Lee, J. Lee, Y. Shin, H. Lee, *Small Sci* **2023**, *3*, 2300063.
[23] P. Strubel, S. Thieme, C. Weller, H. Althues, S. Kaskel, *Nano Energy* **2017**, *34*, 437.
[24] X. Yu, H. Pan, Y. Zhou, P. Northrup, J. Xiao, S. Bak, M. Liu, K.-W. Nam, D. Qu, J. Liu, T. Wu, X.-Q. Yang, *Adv. Energy Mater.* **2015**, *5*, 1500072.
[25] L. Shi, S.-M. Bak, Z. Shadike, C. Wang, C. Niu, P. Northrup, H. Lee, A. Y. Baranovskiy, C. S. Anderson, J. Qin, *Energy Environ. Sci* **2020**, *13*, 3620.
[26] W. J. Weydanz, H. Reisenweber, A. Gottschalk, M. Schulz, T. Knoche, G. Reinhart, M. Masuch, J. Franke, R. Gilles, *J. Power Sources* **2018**, *380*, 126.
[27] L. Gao, S. Han, H. Ni, J. Zhu, L. Wang, S. Gao, Y. Wang, D. Huang, Y. Zhao, R. Zou, *Natl. Sci. Rev.* **2023**, *10*, nwad238.
[28] R. F. Ziesche, N. Kardjilov, W. Kockelmann, D. J. L. Brett, P. R. Shearing, *Joule* **2022**, *6*, 35.
[29] X. Zhang, M. Osenberg, R. F. Ziesche, Z. Yu, J. Kowal, K. Dong, Y. Lu, I. Manke, *ACS Energy Lett.* **2024**, *10*, 496.
[30] J. Yu, I. Pinto-Huguet, C. Y. Zhang, Y. Zhou, Y. Xu, A. Vizintin, J. J. Velasco-Velez, X. Qi, X. Pan, G. Oney, A. Olgo, K. Marker, M. D. S. L, Y. Luo, Y. Lu, C. Huang, E. Hark, J. Fleming, P. Chenevier, A. Cabot, Y. Bai, M. Botifoll, A. P. Black, Q. An, T. Amietszajew, J. Arbiol, *ACS Energy Lett.* **2024**, *9*, 6178.
[31] R. Bradbury, M. A. Kraft, T. Arlt, N. Kardjilov, N. Kardjilov, J. Janek, I. Manke, W. G. Zeier, S. Ohno, *Adv. Energy Mater.* **2023**, *13*, 2203426.
[32] Z. Deng, X. Lin, Z. Huang, J. Meng, Y. Zhong, G. Ma, Y. Zhou, Y. Shen, H. Ding, Y. Huang, *Adv. Energy Mater.* **2020**, *11*, 2000806.
[33] T. Knoche, V. Zinth, M. Schulz, J. Schnell, R. Gilles, G. Reinhart, *J. Power Sources* **2016**, *331*, 267.
[34] B. Michalak, H. Sommer, D. Mannes, A. Kaestner, T. Brezesinski, J. Janek, *Sci. Rep.* **2015**, *5*, 15627.
[35] F. S. Moulder, W. F., P. E. Sobol, *Handbook of X-ray photoelectron spectroscopy, Physical Electronics Division*, Perkin-Elmer Corp, Eden Prairie, Minn., USA, **1992**.
[36] L. Xue, Y. Li, A. Hu, M. Zhou, W. Chen, T. Lei, Y. Yan, J. Huang, C. Yang, X. Wang, Y. Hu, J. Xiong, *Small Struct.* **2022**, *3*, 2100170.
[37] S. Lang, S. H. Yu, X. Feng, M. R. Krumov, H. D. Abruna, *Nat. Commun.* **2022**, *13*, 4811.
[38] A. Rosenman, E. Markevich, G. Salitra, D. Aurbach, A. Garsuch, F. F. Chesneau, *Adv. Energy Mater.* **2015**, *5*, 1500212.
[39] J. B. R. Roby Soni, P. R. Shearing, D. J. L. Brett, A. J. E. Rettie, T. S. Miller, *Energy Storage Mater.* **2022**, *51*, 97.
[40] R. Müller, T. Boenke, S. Dörfler, T. Abendroth, P. Härtel, H. Althues, S. Kaskel, N. Kardjilov, H. Markötter, M. Sintschuk, A. Hilger, I. Manke, S. Risse, *Adv. Energy Mater.* **2025**, *15*, 2404256.
[41] M. Wild, L. O'Neill, T. Zhang, R. Purkayastha, G. Minton, M. Marinescu, G. J. Offer, *Energy Environ. Sci.* **2015**, *8*, 3477.
[42] L. Qie, A. Manthiram, *ACS Energy Lett.* **2016**, *1*, 46.
[43] Y. Yang, S. Risse, S. Mei, C. J. Jafta, Y. Lu, C. Stöcklein, N. Kardjilov, I. Manke, J. Gong, Z. K., M. Ballauff, *Energy Storage Mater.* **2017**, *9*, 96.
[44] P. P. R. M. L. Harks, C. B. Robledo, T. W. Verhallen, P. H. L. Notten, F. M. Mulder, *Adv. Energy Mater.* **2016**, *7*, 1601635.
[45] S. Lu, Y. Chen, X. Wu, Z. Wang, Y. Li, *Sci. Rep.* **2014**, *4*, 4629.
[46] N. Kaden, R. Schlimbach, Á. R. García, K. Dröder, *Batteries* **2023**, *9*, 164.
[47] J. Hagemeister, F. J. Günter, T. Rinner, F. Zhu, A. Papst, R. Daub, *Batteries* **2022**, *8*, 159.
[48] Z. Deng, Z. Huang, Y. Shen, Y. Huang, H. Ding, A. Luscombe, M. Johnson, J. E. Harlow, R. Gauthier, J. R. Dahn, *Joule* **2020**, *4*, 2017.
[49] S. Feng, R. K. Singh, Y. Fu, Z. Li, Y. Wang, J. Bao, Z. Xu, G. Li, C. Anderson, L. Shi, Y. Lin, P. G. Khalifah, W. Wang, J. Liu, J. Xiao, D. Lu, *Energy Environ. Sci.* **2022**, *15*, 3842.
[50] Q. Jin, X. Qi, F. Yang, R. Jiang, Y. Xie, L. Qie, Y. Huang, *Energy Storage Mater.* **2021**, *38*, 255.
[51] W. Tang, Z. Chen, B. Tian, H. W. Lee, X. Zhao, X. Fan, Y. Fan, K. Leng, C. Peng, M. H. Kim, M. Li, M. Lin, J. Su, J. Chen, H. Y. Jeong, X. Yin, Q. Zhang, W. Zhou, K. P. Loh, G. W. Zheng, *J. Am. Chem. Soc.* **2017**,*139*, 10133.
[52] F. Y. Fan, M. S. Pan, K. C. Lau, R. S. Assary, W. H. Woodford, L. A. Curtiss, W. C. Carter, Y.-M. Chiang, *J. Electrochem. Soc.* **2016**, *163*, A3111.
[53] Z. Li, L. P. Hou, N. Yao, X. Y. Li, Z. X. Chen, X. Chen, X. Q. Zhang, B. Q. Li, Q. Zhang, *Angew. Chem. Int. Ed. Engl.* **2023**, *62*, 202309968.
[54] H. J. Peng, J. Q. Huang, X. Y. Liu, X. B. Cheng, W. T. Xu, C. Z. Zhao, F. Wei, Q. Zhang, *J. Am. Chem. Soc.* **2017**, *139*, 8458.
[55] P. Bai, J. Li, F. R. Brushett, M. Z. Bazant, *Energy Environ. Sci.* **2016**, *9*, 3221.
[56] G. M. Hobold, J. Lopez, R. Guo, N. Minafra, A. Banerjee, Y. Shirley Meng, Y. Shao-Horn, B. M. Gallant, *Nat. Energy* **2021**, *6*, 951.
[57] W. Du, R. E. Owen, A. Jnawali, T. P. Neville, F. Iacoviello, Z. Zhang, S. Liatard, D. J. L. Brett, P. R. Shearing, *J. Power Sources* **2022**, *520*, 230818.